PERGAMON

International Journal of Heat and Mass Transfer 43 (2000) 3013–3026

International Journal of HEAT and MASS TRANSFER

www.elsevier.com/locate/ijhmt

Direct simulation of weak laminar plane fountains in a homogeneous fluid

Wenxian Lin*, S.W. Armfield

Department of Mechanical and Mechatronic Engineering, The University of Sydney, Sydney, NSW 2006, Australia

Received 5 October 1998; received in revised form 23 November 1999

Abstract

The behaviour of weak laminar plane fountains that result from the injection of dense fluids upwards into a large container of homogeneous fluid of lower density is studied numerically by using a time-accurate finite volume code. The study is an extension of a previous numerical study on weak laminar axisymmetric fountains. Weak laminar plane fountains with both a uniform and a parabolic profile of the discharge velocity at the source have been investigated. The initial, temporary and final characteristic fountain heights and the times for the fountain front to reach these heights have been determined and scaled. At steady state, a height scale as well as a horizontal length scale for the fountain width are determined. The vertical distribution of the vertical velocity and temperature on the symmetry line are shown to scale with this height. The height and horizontal length scales have been used to scale the horizontal variation of both the horizontal and the vertical velocity in the fountain core at steady state.

1. Introduction

Whenever a dense fluid is injected vertically upward into a miscible and less dense fluid a fountain forms. The denser fluid penetrates to a finite height, whereupon it stops, and falls back as a plunging plume around the upward flow. Surrounding ambient fluid is constantly being entrained into the plunging plume, while the inner rising jet can only entrain into the outer plume fluid. The net result is that, as the injected fluid travels through the ambient fluid, its volumetric flow rate increases and its mean density decreases. Fountains also occur in the reverse case, when lighter fluid is injected vertically downward into a denser ambient fluid.

For fountains with a relatively large discharge momentum compared to the negative buoyancy ($Fr > 1.0$, especially $Fr \gg 1.0$) and large Reynolds numbers, the flow becomes turbulent quite close to the source. There have been many experimental, analytical and numerical studies on turbulent fountains in the past decades [1–16].

When the discharge momentum is less than the negative buoyancy ($Fr < 1.0$) the streamlines curve and spread from the source with no distinguishable strong upward and downward flow. These are denoted weak fountains and are the subject of the present study. Weak fountains occur in the replenishment of cold water in solar ponds [17], in the melting of magna chamber roofs [18] as well as many other environmental and industrial settings.

When Re is not too large, dimensional consistency

* Corresponding author. Tel.: +61-2-9351-2591; fax: +61-2-9351-7060.

E-mail address: lin@orr.mech.eng.usyd.edu.au (W. Lin).

0017-9310/00/$ - see front matter
PII: S0017-9310(99)00366-X

Nomenclature

a_0, a_1	Constants
Fr	Froude number
H, L	Dimensional height and half-width of container
p, P	Nondimensionalized and dimensional pressure
Pr	Prandtl number
R	Regression coefficient
Re	Reynolds number
t	Dimensional time
T	Dimensional temperature
T_0, T_a	Dimensional temperature at source and at ambient
u, U	Nondimensionalized and dimensional x-velocity
v, V	Nondimensionalized and dimensional y-velocity
V_0	Dimensional mean momentum weighted discharge velocity at source
V_m	Dimensional maximum discharge velocity at source
x, X	Nondimensionalized and dimensional horizontal coordinate
x_w	Nondimensionalized fountain width
X_0	Dimensional half-width of the source slot
y, Y	Nondimensionalized and dimensional vertical coordinate
y_m, Y_m	Nondimensionalized and dimensional fountain height
y_{mf}, y_{mi}, y_{mt}	Nondimensionalized final, initial, temporary fountain height

Greek symbols

θ	Nondimensionalized temperature
κ	Thermal conductivity
ν	Kinematic viscosity
ρ	Density
σ_0	Reduced gravity between fountain and ambient
τ	Nondimensionalized time
τ_m	Nondimensionalized time for the fountain front to reach y_m
τ_{mf}, τ_{mi}, τ_{mt}	Nondimensional time to reach y_{mf}, y_{mi}, y_{mt}
Δx_w, Δy_w	Nondimensionalized first grid size in x- and y-direction
$\Delta\tau$	Nondimensionalized time step

requires that

$$\frac{Y_m}{X_0} \sim Fr. \tag{1}$$

where Fr is defined as:

$$Fr = \frac{V_0}{(X_0\sigma_0)^{1/2}}. \tag{2}$$

Recently a numerical investigation of the transient behaviour of weak axisymmetric fountains in a homogeneous fluid has been carried out [19]. In that work, the behaviour of weak axisymmetric fountains with both a uniform and a parabolic profile of the discharge velocity at the fountain source were investigated using a time-accurate finite-volume code. The evolution of the transient fountain flow was analyzed and two distinct stages of evolution identified. The time series of the passage of the fountain front was presented and the initial, temporary and final characteristic fountain heights determined and scaled. At steady state a horizontal length scale which describes the fountain width as well as a height scale, were obtained and together were used to scale the axial and radial profiles of velocity in the fountain core at steady state.

In this paper, the previous study of weak axisymmetric fountains is extended, using the same procedure [19], to investigate the behaviour of weak laminar plane fountains issuing vertically into a quiescent homogeneous ambient fluid. The main differences between axisymmetric and plane fountains are that the latter penetrate to a greater height, have a greater spread and take longer to achieve a steady state. Quantitative differences, such as the exact form of the scaling relations, are detailed below. In Section 2, a brief description of the numerical method used is introduced. Numerical results for $Fr = 1.0$ are presented in Section 3 to provide a qualitative description of the flow. Time series of the passage of the fountain front are then presented to determine the characteristic length scales. In Section 4, the velocity and temperature distributions are analyzed and scaled. Finally, the main conclusions are summarized in Section 5.

2. Numerical method

2.1. Governing equations

The physical domain consists of a container of height H and width $2L$ with non-slip insulated sidewalls and open top. A slot of width $2X_0$ is located at

the centre of the bottom, forming the fountain source, while the rest of the bottom is insulated and non-slip. The fluid is initially isothermal and quiescent at temperature T_a. A stream of fluid at $T_0 < T_a$ is impulsively injected into the container at the source, starting at time $t = 0$, and maintained thereafter. It is assumed that the length of the container is long enough so that two dimensional flow may be assumed. The flow is assumed to be laminar, two dimensional and symmetrical, allowing the computational domain sketched in Fig. 1 to be used.

Both parabolic and uniform source profiles have been used. The parabolic profile is defined as

$$V(X,0) = V_m\left[1 - \left(\frac{X}{X_0}\right)^2\right] \quad \text{for} \quad 0 \le X \le X_0, \tag{3}$$

while the uniform velocity profile is $V(X,0) = V_0$ for $0 \le X \le X_0$. The uniform and parabolic profiles have the same momentum flux when $V_m = \sqrt{15/8}V_0$ and are then considered comparable. The mean momentum weighted discharge velocity for the parabolic profile is defined to be $V_0 = V_m/\sqrt{15/8}$, and therefore the uniform and parabolic fountains will have the same Froude number when their momentum fluxes are equal.

The flow is described by the Navier–Stokes equations and the temperature equation, with the Boussinesq assumption allowing their incompressible forms to be used. The equations are written in conservative, non-dimensional form in Cartesian coordinates as follows:

$$\frac{\partial u}{\partial x} + \frac{\partial v}{\partial y} = 0, \tag{4}$$

$$\frac{\partial u}{\partial \tau} + \frac{\partial (uu)}{\partial x} + \frac{\partial (vu)}{\partial y} = -\frac{\partial p}{\partial x} + \frac{1}{Re}\left(\frac{\partial^2 u}{\partial x^2} + \frac{\partial^2 u}{\partial y^2}\right), \tag{5}$$

$$\frac{\partial v}{\partial \tau} + \frac{\partial (uv)}{\partial x} + \frac{\partial (vv)}{\partial y} = -\frac{\partial p}{\partial y} + \frac{1}{Re}\left(\frac{\partial^2 v}{\partial x^2} + \frac{\partial^2 v}{\partial y^2}\right) + \frac{1}{Fr^2}\theta, \tag{6}$$

$$\frac{\partial \theta}{\partial \tau} + \frac{\partial (u\theta)}{\partial x} + \frac{\partial (v\theta)}{\partial y} = \frac{1}{RePr}\left(\frac{\partial^2 \theta}{\partial x^2} + \frac{\partial^2 \theta}{\partial y^2}\right), \tag{7}$$

with Re and Pr defined respectively as follows:

$$Re = \frac{V_0 X_0}{\nu}, \qquad Pr = \frac{\nu}{\kappa}. \tag{8}$$

The following nondimensionalization is used:

$$x = \frac{X}{X_0}, \quad y = \frac{Y}{X_0}, \quad u = \frac{U}{V_0}, \quad v = \frac{V}{V_0}, \quad \tau = \frac{t}{(X_0/V_0)}, \quad p = \frac{P}{\rho V_0^2}, \quad \theta = \frac{T - T_a}{T_0 - T_a}, \tag{9}$$

nondimensionalizationwith initial and boundary conditions,

$$u = v = 0, \theta = 0, \quad \text{at all} \quad x, y \quad \text{and} \quad \tau < 0; \tag{10}$$

and

$$u = 0, \frac{\partial v}{\partial x} = 0, \frac{\partial \theta}{\partial x} = 0 \quad \text{on} \quad x = 0, 0 \le y \le H/X_0;$$

$$u = v = 0, \frac{\partial \theta}{\partial x} = 0, \quad \text{on} \quad x = L/X_0, 0 \le y \le H/X_0;$$

$$u = 0, v = v(x,0), \theta = -1 \quad \text{on} \quad 0 \le x \le 1, y = 0;$$

$$u = v = 0, \frac{\partial \theta}{\partial y} = 0, \quad \text{on} \quad 1 < x \le L/x_0, y = 0;$$

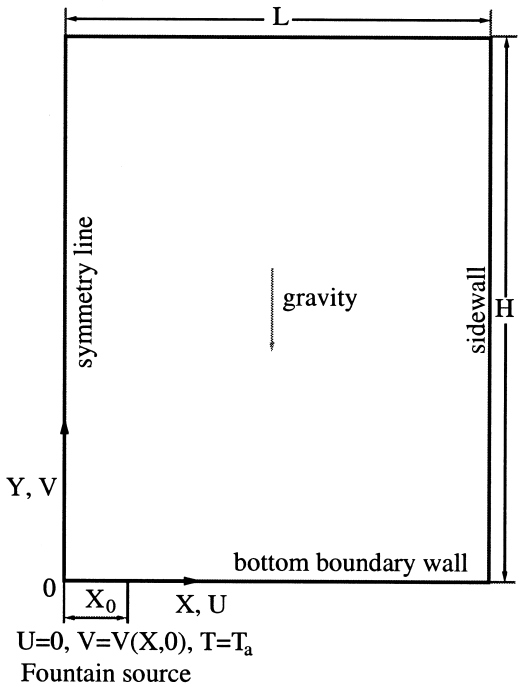

Fig. 1. Computational domain and coordinate system.

$$\frac{\partial u}{\partial y} = \frac{\partial v}{\partial y} = \frac{\partial \theta}{\partial y} = 0 \quad \text{on} \quad 0 \le x \le L/X_0, \quad y = H/X_0, \tau \ge 0. \tag{11}$$

In this study, H has been chosen to be large enough with respect to X_0 ($H/X_0 = 15$) so that the upper ($y = H/X_0$) boundary has little influence on the fountain flow and the assumption of parallel flow conditions at the upper boundary in Eq. (11) is appropriate. Unless otherwise specified $Pr = 7$, $Re = 200$ and $H = L = 15X_0$ are used in all the numerical simulations in this study.

2.2. Discretization and time integration

The mesh concentrates points in the fountain region and in the boundary layers and is relatively coarse in other regions. A uniform fine mesh is used in the regions $0 \le \times \le 2$ and $0 \le y \le 2$ with a stretched mesh in the remaining region both in the x- and y-directions. $H/X_0 = L/X_0 = 15$ and $\Delta x_w = \Delta y_w = 3 \times 10^{-2}$ are used, which results in 66 cells in the uniform mesh region in both directions. The meshes beyond $x = 2$ and $y = 2$ expand at a rate of 7.6% up to $x = 0.1(L/X_0 - 2)$ or $y = 0.1(H/X_0 - 2)$. Beyond $x = 0.1(L/X_0 - 2)$ or $y = 0.1(H/X_0 - 2)$, the mesh size expansion rate decreases at a rate of 10% until it reaches zero, resulting in a constant coarse mesh in the remaining region, giving 145×145 volumes in the computational domain shown in Fig. 1.

The equations are discretized on a non-staggered mesh using finite volumes, with standard second-order central differences used for the viscous, the pressure gradient and divergence terms. The QUICK third-order upwind scheme [20] is used for the advective terms. The momentum and temperature equations are solved using an ADI scheme. The second-order Adams–Bashforth scheme and Crank–Nicholson scheme are used for the time integration of the advective terms and the diffusive terms, respectively. To enforce continuity, the pressure correction method is used to construct a Poisson's equation which is solved using the preconditioned GMRES method. Detailed descriptions of these schemes can been found in [21–23] and the code has been previously used for the simulation of buoyancy dominated flows [24–28].

2.3. Grid independence

Grid independence is tested by comparing the solution obtained on the basic mesh of 145×145 volumes defined above, with $\Delta\tau = 5 \times 10^{-4}$, with those obtained on two additional fine meshes, with the following parameters. In the first fine mesh, $\Delta x_w = \Delta y_w = 1.5 \times 10^{-2}$ but the grid expansion factor and the time step ($\Delta\tau = 5 \times 10^{-4}$) are not changed, which gives a mesh of 225×225 volumes. In the second fine mesh, $\Delta x_w = \Delta y_w = 1.25 \times 10^{-2}$ and $\Delta\tau = 0.25 \times 10^{-4}$ but the same grid expansion factor is still used, giving a mesh of 257×257 volumes. The variation between the three solutions is very small, as can be seen in Fig. 2, indicating that the basic mesh and time step are providing sufficient resolution.

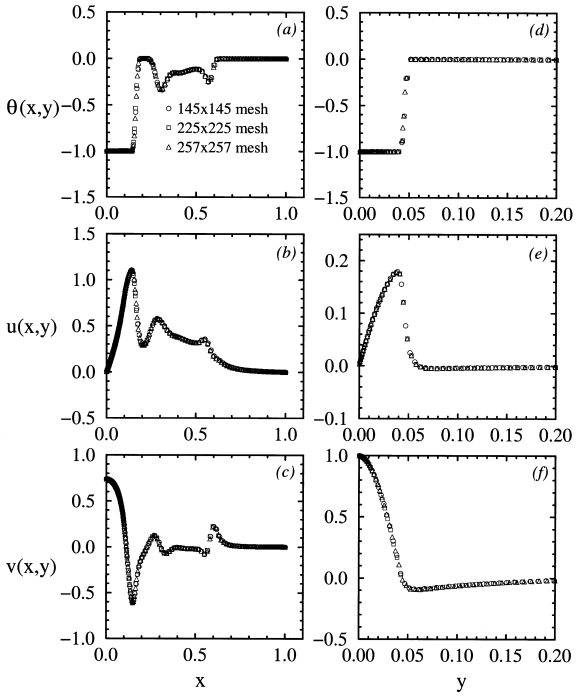

Fig. 2. Comparison of the results from the 145×145, 225×225 and 257×257 meshes: (a), (b) and (c), horizontal profiles of temperature and velocities at $y = 0.0208$; (d), (e) and (f), vertical profiles of temperature and velocities at $x = 0.0208$ when $\tau = 1.0$, respectively.

3. Evolution of transient fountain flow

3.1. Qualitative observations

An overview of the time evolution of the flow is shown in Fig. 3, which presents temperature contours for $Fr = 1.0$ with uniform profile. After initiation the fountain grows until the momentum of the rising fluid is balanced by the negative buoyancy, coming to rest at an initial characteristic fountain height, y_{mi}, approximately at $\tau = 2.2$. The rising flow begins to spread outwards immediately after discharge due to its reduced velocity and interaction with the ambient fluid. After the fountain front reaches y_{mi} the down-

flowing fluid interacts with the environment and with the upflow, restricting the rise of further fluid and reducing y_{mi} to a smaller value, y_{mt}, the temporary characteristic fountain height. As the downflow fluid always remains denser than the ambient in a homogeneous ambient, it spreads along the bottom floor of the container, forming an eddy in the region bounded by the upflow, downflow and the floor and an intrusion moving outwards along the floor. This eddy initially contains ambient fluid which is gradually dissipated as the flow develops. The fountain front subsequently rises to a height y_{mf}, which is a little larger than y_{mi}, at $\tau = 15.5$ and it stays at this height thereafter. The upflow and downflow are steady and the only unsteady flow is the spreading of the intrusion along the bottom floor of the container, and y_{mf} is the final characteristic fountain height. This flow evolution is similar to that observed for weak axisymmetric fountains [19] in which y_{mf} is slightly smaller that y_{mi}, and for turbulent fountains [4,13,14,16] although there the ratio of the initial to final fountain height is 1.43, much larger than for weak laminar fountains. Similar flow patterns are also observed with weak laminar plane fountains when the discharge velocity at the source has the parabolic profile represented by Eq. (3).

3.2. Quantitative observations

3.2.1. Characteristic fountain heights

In the previous experimental studies on turbulent fountains, the final characteristic fountain height y_{mf} is usually used as the maximum fountain penetration height. As the initial and temporary characteristic fountain heights also describe the behaviour of the fountains, especially for weak fountains where the fountain heights are of the same order as the width of the source, it is worthwhile to consider them too.

An explicit form of Eq. (1) for weak laminar plane

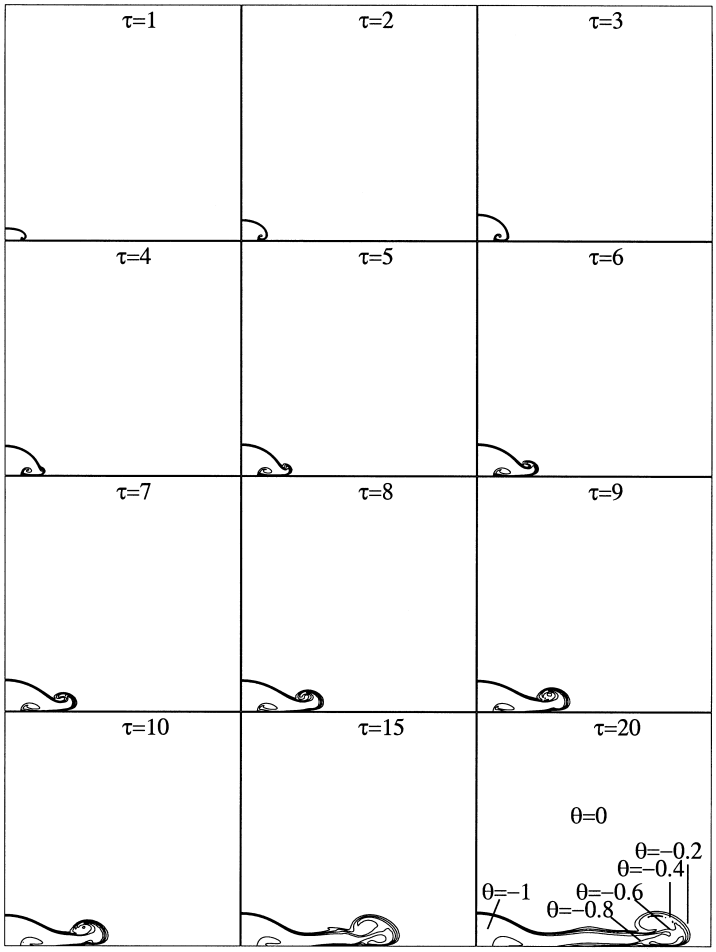

Fig. 3. A typical time evolution of the transient temperature contours for $Fr = 1.0$ with the uniform profile.

fountains is obtained by plotting initial, temporary and final height against Fr for $0.1 \le Fr \le 1.0$, as shown in Fig. 4. Results are presented for both the uniform and parabolic profiles, and a linear fit of the form

$$y_m = a_0 + a_1 Fr, \tag{12}$$

has been obtained for each of the sets of data in the range $0.2 \le Fr \le 1.0$, where y_m represents y_{mi}, y_{mt} and y_{mf} respectively. The values of a_0 and a_1, obtained by regression from the numerical results, are listed in Table 1.

It is found that a weak plane fountain penetrates to a greater height than a weak axisymmetric fountain, for which $y_{mf} = 0.198 + 1.165Fr$ for the uniform profile and $y_{mf} = 0.105 + 1.018Fr$ for the parabolic profile.

The linear fit provides a good representation of the data for $0.2 \le Fr \le 1.0$, with some departure for $Fr < 0.2$, while for Fr tending to zero the linear fit does not tend to zero, which is clearly not physical. This was also observed for weak axisymmetric fountains.

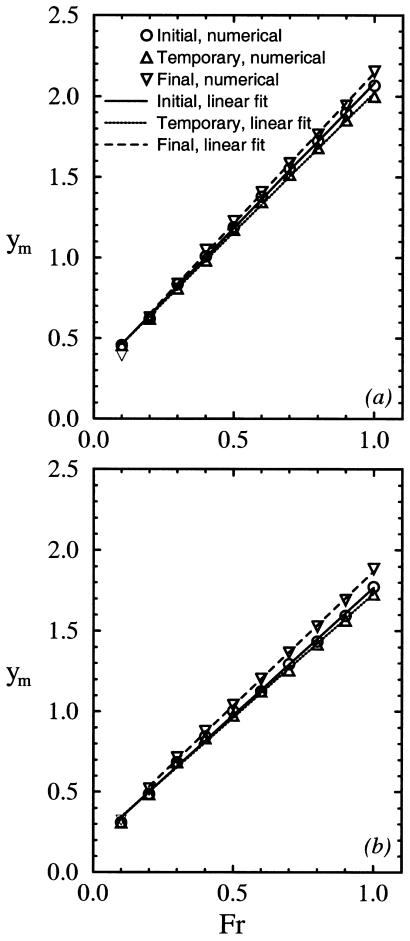

Fig. 4. Initial, temporary and final fountain heights plotted against Fr with (a) the uniform profile and (b) the parabolic profile.

Table 1
Regression results of Eq. (12) for both the uniform and parabolic profiles

Profile	y_m	a_0	a_1	R
uniform	y_{mi}	0.2832 ± 0.0089	1.7992 ± 0.0144	0.9997
	y_{mt}	0.2890 ± 0.0094	1.7355 ± 0.0152	0.9997
	y_{mf}	0.2774 ± 0.0130	1.8696 ± 0.0199	0.9996
parabolic	y_{mi}	0.1838 ± 0.0147	1.5548 ± 0.0235	0.9990
	y_{mt}	0.1927 ± 0.0143	1.5382 ± 0.0231	0.9990
	y_{mf}	0.2015 ± 0.0096	1.6693 ± 0.0148	0.9997

When $Fr > 1.0$, the characteristic fountain heights of laminar plane fountains increase more rapidly than is predicted by Eq. (12), as was also observed for weak axisymmetric fountains [19]. The fountain discharge momentum at the source then dominates buoyancy and the entrainment between the fountain and the surrounding ambient fluid becomes important. Fountains with $Fr > 1$ are regarded as strong fountains with different scaling relations and are beyond the scope of this study.

3.2.2. Time scales for the fountain front

As shown in [19], dimensional consistency requires that τ_m is scaled in terms of Fr as:

$$\tau_m \sim Fr^2 \tag{13}$$

The numerically simulated τ_m plotted against Fr^2 for $0.2 \le Fr \le 1.0$ are shown in Fig. 5, confirming the scaling which is well predicted by the following explicit form:

$$\tau_m = a_0 + a_1 Fr^2, \tag{14}$$

where the values of a_0 and a_1, which have been obtained by regression from the numerical results, are listed in Table 2.

Table 2
Regression results of Eq. (14) for both the uniform and parabolic profiles

Profile	t_m	a_0	a_1	R
uniform	t_{mi}	1.020 ± 0.030	4.992 ± 0.056	0.9996
	t_{mt}	1.326 ± 0.037	7.700 ± 0.070	0.9997
	t_{mf}	1.601 ± 0.084	14.059 ± 0.159	0.9996
parabolic	t_{mi}	0.727 ± 0.043	3.325 ± 0.080	0.9977
	t_{mt}	0.978 ± 0.018	4.864 ± 0.033	0.9998
	t_{mf}	1.211 ± 0.032	9.925 ± 0.060	0.9998

Compared to weak axisymmetric fountains for which $\tau_{mf} = 0.669 + 8.146Fr^2$ for the uniform profile and $\tau_{mf} = 0.305 + 4.415Fr^2$ for the parabolic profile, plane fountains need a much longer time to reach the final fountain height and thus to achieve steady state.

3.3. Fountain width

The fountain flow is steady when $\tau > \tau_{mf}$ and a characteristic fountain width can be determined for each Fr. Fig. 6 presents the x distribution of $v(x, y)$ for both the uniform and parabolic profiles for $Fr = 1.0$ at different heights. At each height, $v(x, y)$ decreases gradually as x increases until at a specific x where $v(x, y)$ becomes zero for each y, where the upflow terminates and the downflow begins. $v(x, y)$ continues to reduce beyond this location until a clearly defined minimum is reached, then increasing until it again crosses the zero line. A clearly defined minimum exists for the envelope of the minima, corresponding to the $y = 0.5y_{mf}$ minimum, which occurs at $x \cong 2.8$ for $Fr = 1.0$ with the uniform profile. The minimum of the envelope always corresponds to the $y = 0.5y_{mf}$ profile minimum and is clearly defined for all Fr considered. The horizontal length scale x_w is defined to be equal to this width, which characterizes the fountain width at steady state. This definition of x_w corresponds very closely to the location of the fountain boundary temperature contours at the origin of the intrusion flow at $y = 0.5y_{mf}$. Obtaining a consistent fountain width directly from the temperature contours is difficult owing to the smooth transformation from fountain to intrusion, whereas the very well defined minimum in the envelope of the minima of the vertical velocity profiles makes the procedure straightforward.

Based on dimensional considerations x_w, like y_m,

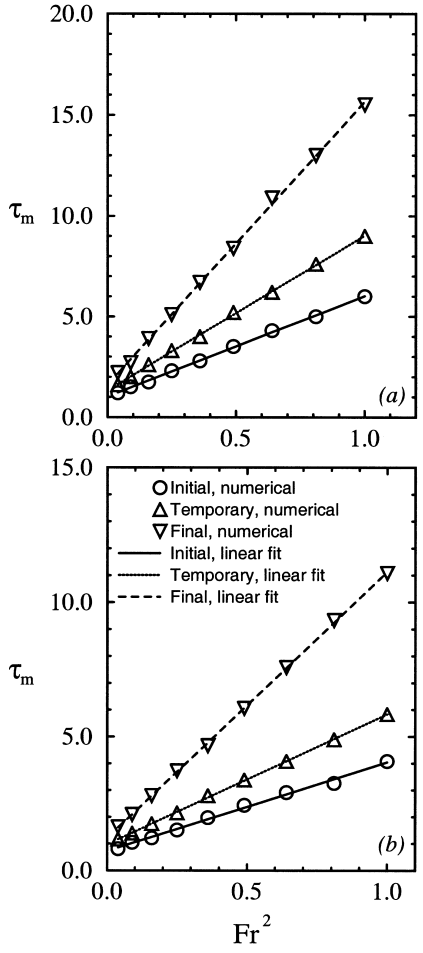

Fig. 5. Times for the fountain front to reach the initial, temporary and final fountain heights plotted against Fr^2 with (a) the uniform profile and (b) the parabolic profile.

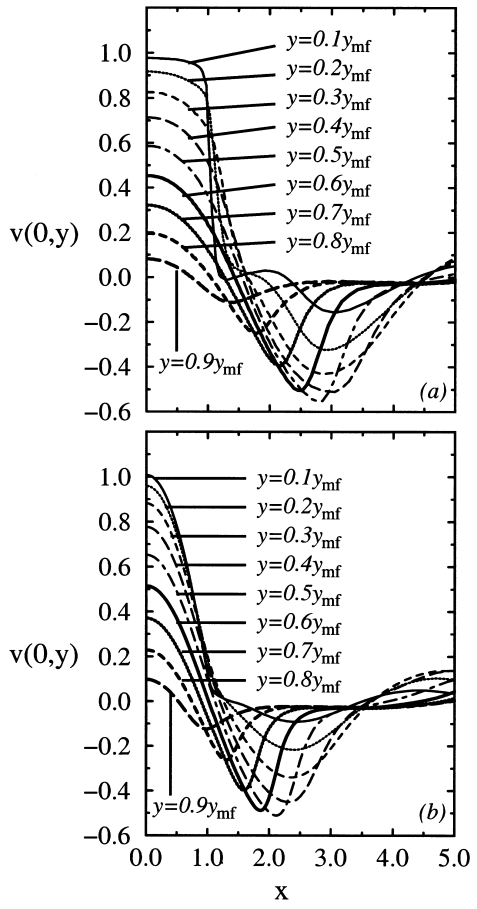

Fig. 6. Horizontal distribution of $v(x, y)$ at different heights for $Fr = 1.0$ with (a) the uniform profile and (b) the parabolic profile.

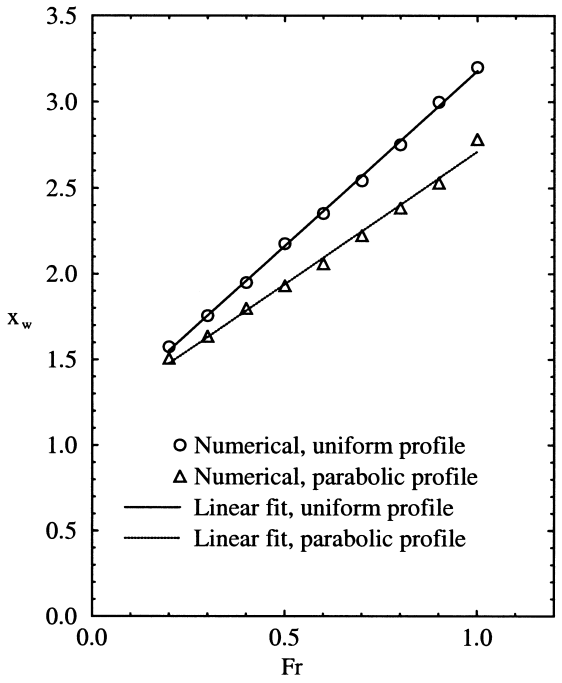

Fig. 7. Fountain width x_w plotted against Fr for $0.2 \le Fr \le 1.0$.

should be of the form $x_w \sim Fr$. Fig. 7 presents x_w plotted against Fr for both the uniform and parabolic profiles with $0.2 \le Fr \le 1.0$. A linear relation clearly exists between x_w and Fr, that is,

$$x_w = a_0 + a_1 Fr, \tag{15}$$

with the values of a_0 and a_1 listed in Table 3, together with the regression coefficients. Compared to weak axisymmetric fountains for which $x_w = 1.1228 + 0.7308Fr$ for the uniform profile and $x_w = 1.0468 + 0.2525Fr$ for the parabolic profile, plane fountains have considerably larger horizontal length scales.

It is expected that these length scales can be used to parameterize the core flow, that is the region bounded by $x = x_w$ and $y = y_{mf}$, as they do for weak axisymmetric fountains [19]. Further discussion of the core region is presented in Section 4.

Table 3
Regression results of Eq. (15) for both the uniform and parabolic profiles

Profile	a_0	a_1	R
uniform	1.1485 ± 0.0149	1.6625 ± 0.0228	0.9993
parabolic	1.1692 ± 0.0194	1.0177 ± 0.0297	0.9968

4. Steady flow patterns in the fountain core

4.1. Vertical distribution

4.1.1. Vertical velocity

In [19], it was shown that the final fountain height provides the appropriate scaling for the vertical velocity in the vertical direction for a weak axisymmetric fountain. Similarly, it is expected that y_{mf} should also provide the appropriate scaling for $v(0, y)$ in the y-direction for weak laminar plane fountains, that is,

$$v(0, y) = f\left(\frac{y}{y_{mf}}\right). \tag{16}$$

Fig. 8 presents results which show the relation between

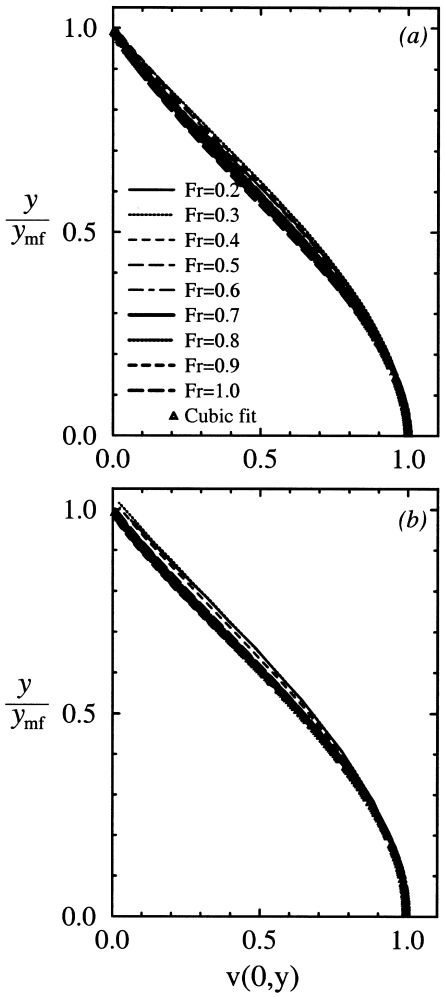

Fig. 8. $v(0, y)$ plotted against y/y_{mf} for $0.2 \le Fr \le 1.0$ with (a) the uniform profile (b) the parabolic profile.

$v(0, y)$ and y/y_{mf} for a series of Fr in the range $0.2 \le Fr \le 1.0$ for both the uniform and parabolic profiles. All the data sets are collapsed onto a single curve and it is therefore clear that y_{mf} does provide the appropriate length scale for the vertical velocity at the symmetry line. A cubic was found to be the lowest order polynomial to provide a good fit to this relation, with the following explicit form for the uniform profile:

$$v(0, y) = 1.0000 - 0.0152\left(\frac{y}{y_{mf}}\right) - 2.0239\left(\frac{y}{y_{mf}}\right)^2 + 1.0349\left(\frac{y}{y_{mf}}\right)^3. \quad (17)$$

and for the parabolic profile,

$$v(0, y) = 1.3693 + 0.1053\left(\frac{y}{y_{mf}}\right) - 2.8146\left(\frac{y}{y_{mf}}\right)^2 + 1.3499\left(\frac{y}{y_{mf}}\right)^3. \quad (18)$$

Values of 0.9967 and 0.9972 were obtained for the regression coefficient squares for these empirical relations.

4.1.2. Vertical temperature variation

As can be seen in Fig. 3 most of the temperature variation at $Pr = 7$ occurs in a very thin layer which is nearest to the fountain front. This indicates negligible entrainment between the ambient fluid and the fountain. Fig. 9, which shows $\theta(0, y)$ plotted against y/y_{mf} for $0.2 \le Fr \le 1.0$, demonstrates that y_{mf} is the appropriate length scale for $\theta(0, y)$, that is,

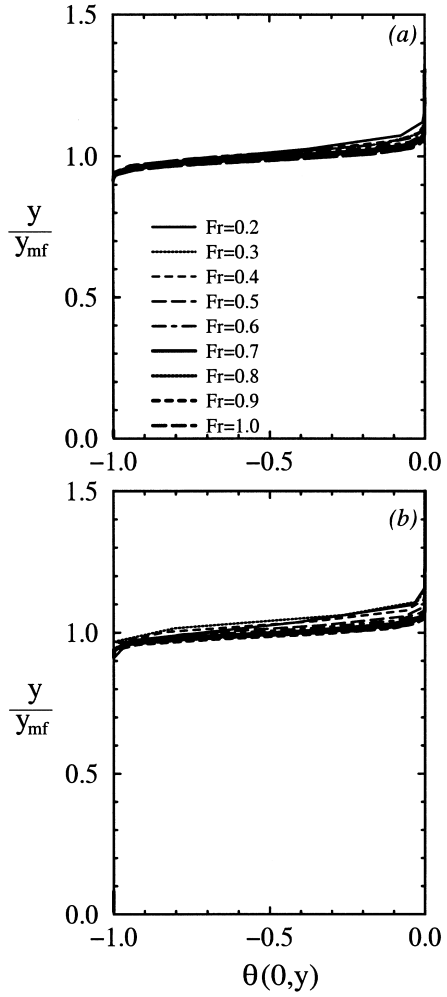

Fig. 9. $\theta(0, y)$ plotted against y/y_{mf} for $0.2 \le Fr \le 1.0$ with (a) the uniform profile (b) the parabolic profile.

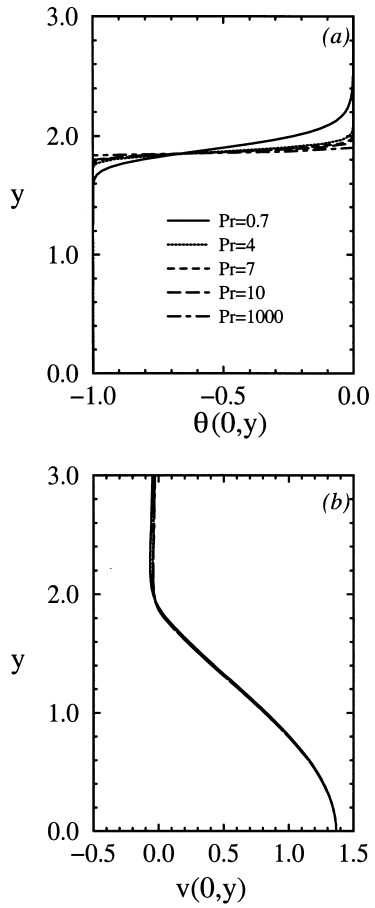

Fig. 10. Vertical distribution of (a) $\theta(0, y)$ and (b) $v(0, y)$ for different Pr when $Fr = 1.0$ with the parabolic profile.

$$\theta(0, y) = f\left(\frac{y}{y_{mf}}\right). \quad (19)$$

4.1.3. Influence of Pr

It is expected that a reduction in Pr will lead to a thicker region over which the temperature varies at the fountain front and when Pr becomes larger, the thickness of the temperature variation will become smaller, approaching zero as $Pr \to \infty$. Fig. 10 shows the temperature and velocity variations on the symmetry line for $0.7 \le Pr \le 1000$ at $Fr = 1.0$ with the parabolic profile. The variation in the temperature layer thickness is clearly seen, whereas the influence of Pr on the velocity profile is very small.

4.2. Horizontal distribution

4.2.1. Zones of establishment and self-similarity

Fig. 6 which shows the horizontal distribution of vertical velocity at a range of heights clarifies that the fountain flow is fully established for $y/y_{mf} \ge 0.55$ and a zone of self-similarity exists for $0.55 \le y/y_{mf} \le 0.8$. The self-similarity collapses for $y/y_{mf} \ge 0.8$ until $y/y_{mf} = 1.0$.

4.2.2. Horizontal distribution of vertical velocity in the zone of self-similarity

As shown in [19] for weak laminar axisymmetric fountains, the vertical velocity $v(x, y)$ should have a height scale of y_{mf} in the zone of self-similarity, while the appropriate width scale is expected to be x_w. It is

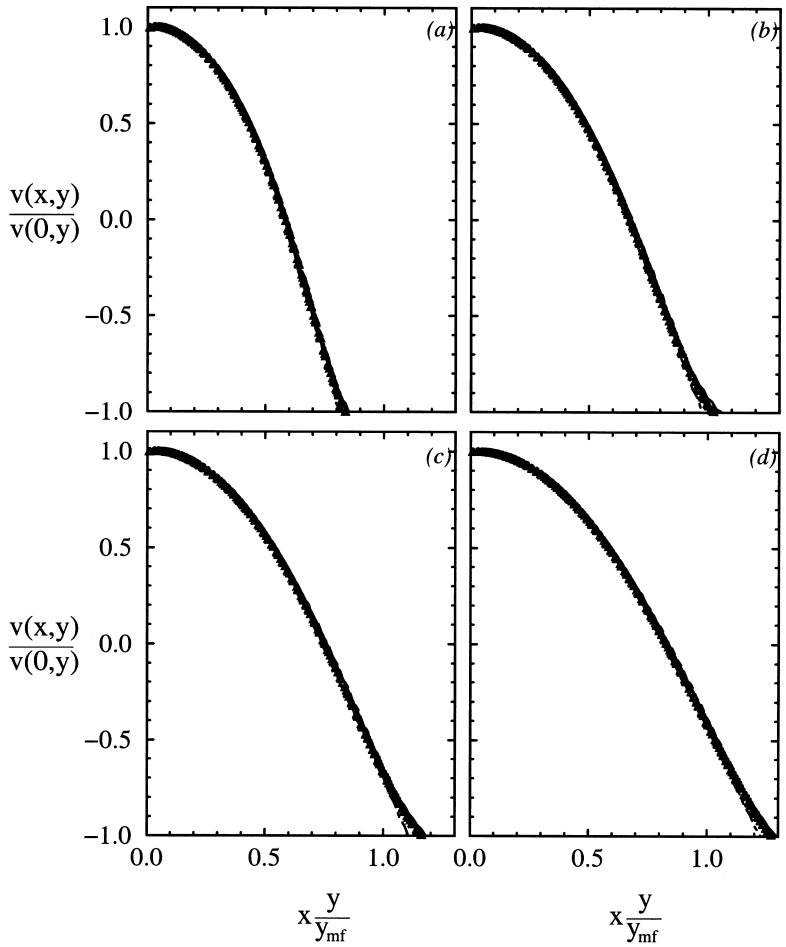

Fig. 11. $v(x, y)/v(0, y)$ plotted against xy/y_{mf} for (a) $Fr = 0.3$; (b) $Fr = 0.5$; (c) $Fr = 0.7$; and (d) $Fr = 0.9$ with the uniform profile: ———, $y/y_{mf} = 0.6$; · · · · · ·, $y/y_{mf} = 0.65$; – – –, $y/y_{mf} = 0.7$; – · –, $y/y_{mf} = 0.75$; △, 5th degree-fit.

therefore expected that a relation will exist between $v(x, y)/v(0, y)$, x/x_w and y/y_{mf}, that is,

$$\frac{v(x, y)}{v(0, y)} = f\left(\frac{x}{x_w}, \frac{y}{y_{mf}}\right). \tag{20}$$

Numerical simulations have been conducted for a series of Fr to provide an explicit form for Eq. (20). $v(x, y)/v(0, y)$ is plotted against xy/y_{mf} for several y/y_{mf} and Fr with the uniform profile in Fig. 11 to determine the relation between $v(x, y)/v(0, y)$ and y/y_{mf}. Each set of results is collapsed onto a single curve by y/y_{mf} scaling and a 5th degree polynomial is the lowest order polynomial which provides a good fit for that data. $v(x, y)/v(0, y)$ is plotted against x/x_w at fixed y/y_{mf} for a range of Fr in Fig. 12, which shows that the x_w scaling collapses the Fr variation in $v(x, y)$ onto a single curve at each y, which is well represented by a cubic fit.

Similar results are also obtained for the parabolic profile. Therefore, a general correlation should exist between $v(x, y)/v(0, y)$ and $(x/x_w)(y/y_{mf})$. Fig. 13 contains $v(x, y)/v(0, y)$ plotted against $(x/x_w)(y/y_{mf})$ for a range of Fr and y_{mf} values for both the uniform and parabolic profiles. All the results are collapsed close to single curves by the y_{mf} and x_w scalings, and are well represented by cubic fits of the form:

$$\frac{v(r, z)}{v(0, z)} = 0.992 + 1.216\left(\frac{x}{x_w}\frac{y}{y_{mf}}\right) - 12.54\left(\frac{x}{x_w}\frac{y}{y_{mf}}\right)^2 + 7.937\left(\frac{x}{x_w}\frac{y}{y_{mf}}\right)^3, \tag{21}$$

for the uniform profile and

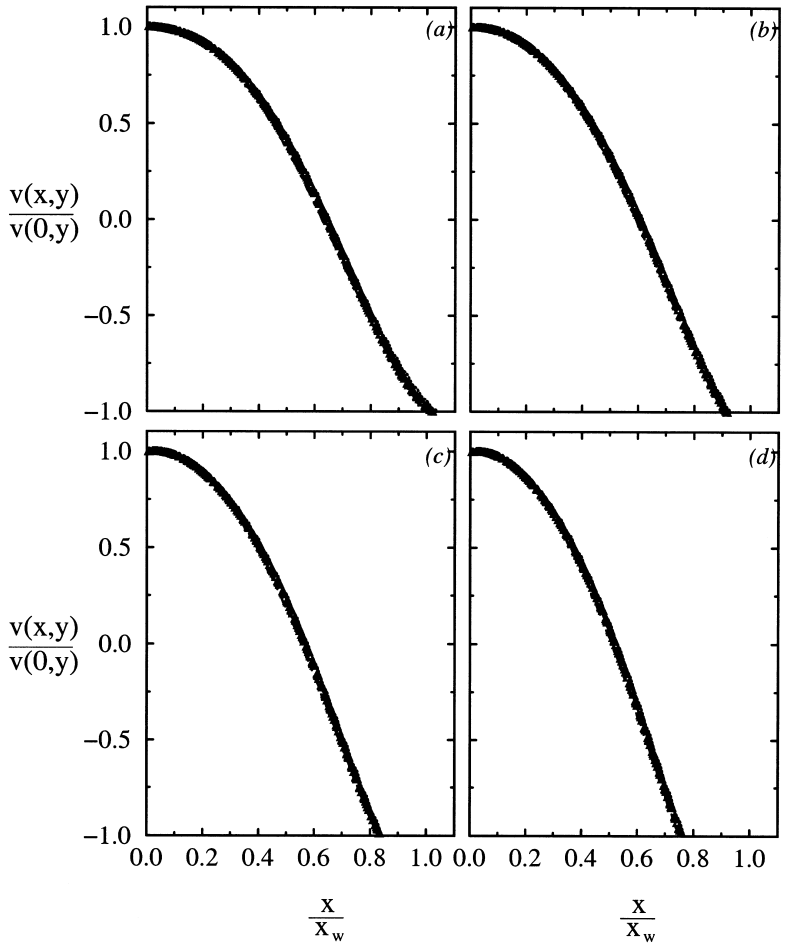

Fig. 12. $v(x, y)/v(0, y)$ plotted against x/x_w for (a) $y/y_{mf} = 0.6$; (b) $y/y_{mf} = 0.65$; (c) $y/y_{mf} = 0.7$; and (d) $y/y_{mf} = 0.75$ with the uniform profile: ———, $Fr = 0.3$; ·····, $Fr = 0.5$; – – –, $Fr = 0.7$; – · –, $Fr = 0.9$; △, cubic-fit.

$$\frac{v(r,z)}{v(0,z)} = 0.993 + 0.624\left(\frac{x}{x_w}\frac{y}{y_{mf}}\right) - 16.26\left(\frac{x}{x_w}\frac{y}{y_{mf}}\right)^2 + 14.894\left(\frac{x}{x_w}\frac{y}{y_{mf}}\right)^3, \quad (22)$$

for the parabolic profile. The square of the regression coefficients of these two correlations are 0.9956 and 0.9947 respectively.

4.2.3. Horizontal distribution of horizontal velocity in the self-similar zone

The horizontal velocity has a maximum value, $u_m(y)$, at each height, and it is expected that in the zone of self-similarity $u(x,y)/u_m(y)$ will be scaled by x_w and y_{mf}. This is shown in Fig. 14 where $u(x,y)/u_m(y)$ is plotted against $x/x_w y/y_{mf}$ for a range of Fr with the uniform profile. All the results are collapsed close to a single curve in the region of the fountain core for each of the data sets for the uniform profile, indicating that x_w and y_{mf} do provide a good parameterisation. Similar results were also obtained for the parabolic profile.

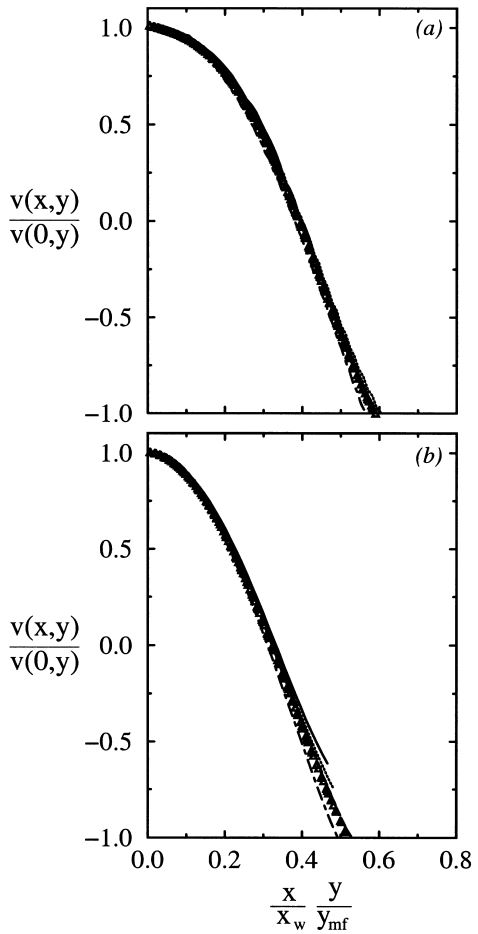

Fig. 13. $v(x,y)/v(0,y)$ plotted against $(x/x_w)(y/y_{mf})$ with (a) the uniform profile and (b) the parabolic profile: ———, $Fr = 0.3$ and $y/y_{mf} = 0.6$; ·····, $Fr = 0.5$ and $y/y_{mf} = 0.65$; – – –, $Fr = 0.7$ and $y/y_{mf} = 0.7$; – · –, $Fr = 0.9$ and $y/y_{mf} = 0.75$; △, cubic-fit.

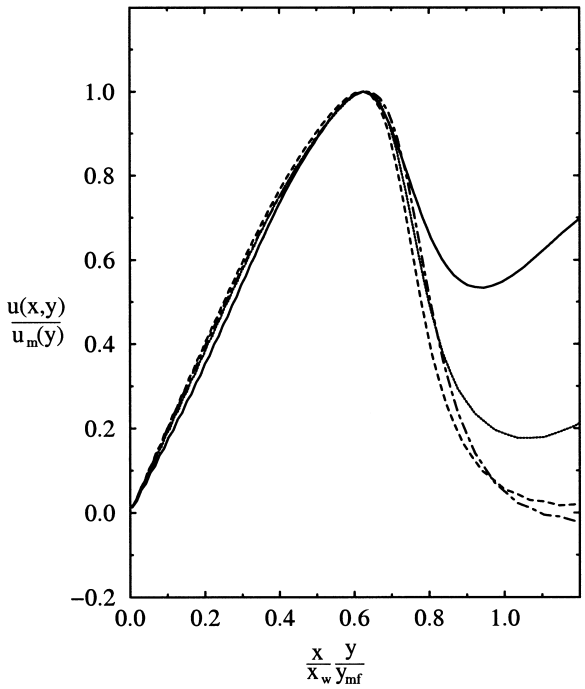

Fig. 14. $u(x,y)/u_m(y)$ plotted against $(x/x_w)(y/\mathrm{mf})$ with the uniform profile: ———, $Fr = 0.3$ and $y/y_{mf} = 0.6$; ·····, $Fr = 0.5$ and $y/y_{mf} = 0.65$; – – –, $Fr = 0.7$ and $y/y_{mf} = 0.7$; – · –, $Fr = 0.9$ and $y/y_{mf} = 0.75$.

5. Conclusions

Weak laminar plane fountains discharged upwards into a homogeneous environment were investigated following the same procedure as used in a previous numerical study of weak axisymmetric fountains. The behaviour of weak laminar plane fountains with both uniform and parabolic discharge velocity profiles at the source was investigated.

A qualitative observation has been made with visualisation of a typical time evolution of the transient temperature contours of a weak laminar plane fountain with $Fr = 1.0$ and the uniform profile. An initial unsteady growth stage and a final steady state have been identified with distinct flow behaviours.

Using dimensional and numerical results explicit correlations were obtained for the initial, temporary and final characteristic fountain heights, in terms of Fr.

These results show that *Fr* is the appropriate control parameter, confirming the dimensional analysis. It has also been shown that the time scale for the development of the fountain flow is a quadratic function of the Froude number and the *Fr* relation for the achievement of steady state has been obtained. This is the same behaviour as that observed with weak axisymmetric fountains, however the exact form of the relation is different with the weak plane fountains achieving a y_{mf} approximately 55% greater than the axisymmetric fountains. Additionally for the axisymmetric fountains $y_{mf} < y_{mi}$ whereas for the plane fountains $y_{mf} > y_{mi}$.

A horizontal length scale, x_w, has been obtained characterising the fountain width and has been shown to be linearly dependent on *Fr*, again confirming the dimensional arguments. The vertical velocity on the symmetry line has been shown to scale with the fountain height, y_{mf}. Both the vertical and horizontal velocities in the fountain core in the region $0.55 \leq y \leq 0.8$ are completely parameterized by y_{mf} and x_w, showing that in this region the flow is self similar. Below the region of self similarity is a zone of establishment, while above the region the self similarity gradually collapses. Compared to axisymmetric fountains, plane fountains have a 52% greater width.

Results presented in this paper were all obtained with $Re = 200$, however additional results have been obtained with $200 \leq Re \leq 800$to determine any *Re* dependency. It was found that there was very little *Re* variation in the results indicating that weak laminar plane fountain flow in this range of *Re* is governed by a balance between buoyancy and advection as predicted by the dimensional analysis, which again indicates that *Fr* is the appropriate control parameter.

The concluding remark from this study is that the behaviour of weak laminar plane fountains is similar to that of weak laminar axisymmetric fountains, although there are quantitative differences between them.

Acknowledgements

We are very grateful for the reviewers' comments which helped us to clarify some important points and improve the quality of the paper significantly. The financial support of an AusAID Scholarship and from the National Natural Science Foundation and Yunnan Province of the People's Republic of China for W. Lin is gratefully acknowledged.

References

[1] B.R. Morton, Forced plumes, J. Fluid Mech 5 (1959) 151–163.
[2] B.R. Morton, The ascent of turbulent forced plumes in a calm atmosphere, Int. J. Air Poll 1 (1959) 184–197.
[3] G. Abraham, Jets with negative buoyancy in homogeneous fluid, J. Hydraulic Res 5 (1967) 235–248.
[4] J.S. Turner, Jets and plumes with negative or reversing buoyancy, J. Fluid Mech 26 (1966) 779–792.
[5] J.S. Turner, Buoyancy Effects in Fluids, Cambridge University Press, Cambridge, 1973.
[6] R.A. Seban, M.M. Behnia, K.E. Abreau, Temperatures in a heated air jet discharged downward, Int. J. Heat Mass Transfer 21 (1978) 1453–1458.
[7] H.B. Fischer, E.J. List, R.C.Y. Koh, J. Imberger, N.H. Brooks, Mixing in Inland and Coastal Waters, Academic, New York, 1979.
[8] C.J. Chen, W. Rodi, Vertical Turbulent Buoyant Jets, Pergamon, Oxford, 1980.
[9] W. Rodi, Turbulent Buoyant Jets and Plumes, Pergamon, Oxford, 1982.
[10] E.J. List, Turbulent jets and plumes, Ann. Rev. Fluid Mech 14 (1982) 189–212.
[11] T. Mizushina, F. Ogino, H. Takeuchi, H. Ikawa, An experimental study of vertical turbulent jet with negative buoyancy, Wärme- und Stoffübertragung 16 (1982) 15–21.
[12] J.S. Turner, Turbulent entrainment: the development of the entrainment assumption, and its application to geophysical flows, J. Fluid Mech 173 (1986) 431–471.
[13] I.H. Campbell, J.S. Turner, Fountains in magma chambers, J. Petrol 30 (1989) 885–923.
[14] W.D. Baines, J.S. Turner, I.H. Campbell, Turbulent fountains in an open chamber, J. Fluid Mech 212 (1990) 557–592.
[15] W.D. Baines, A.F. Corriveau, T.J. Reedman, Turbulent fountains in a closed chamber, J. Fluid Mech 255 (1993) 621–646.
[16] L.J. Bloomfield, R.C. Kerr, Turbulent fountains in a stratified fluid, J. Fluid Mech 358 (1998) 335–356.
[17] J.A. Duffie, W.A. Beckman, Solar Engineering of Thernal Processes, 2nd ed, Wiley, New York, 1991.
[18] H.E. Huppert, R.S.J. Sparks, Melting the roof of a chamber containing a hot, turbulently convecting fluid, J. Fluid Mech 188 (1988) 107–131.
[19] W. Lin, S.W. Armfield, Direct simulation of weak axisymmetric fountains in a homogeneous fluid, J. Fluid Mech. 403 (2000) 67–88.
[20] B.P. Leonard, A stable and accurate convective modelling procedure based on quadratic upstream interpolation, Comput. Meth. Appl. Mech. Engng 19 (1979) 59–98.
[21] S.W. Armfield, Finite-difference solutions of the Navier–Stokes equations on staggered and non-staggered grids, Computers and Fluids 20 (1991) 1–17.
[22] S.W. Armfield, Ellipticity, accuracy, and convergence of the discrete Navier–Stokes equations, J. Computational Physics 114 (1994) 176–184.
[23] S.W. Armfield, R. Street, The fractional-step method for the Navier–Stokes equations on staggered grids: the

accuracy of three variations, J. Computational Physics 153 (1999) 660–665.
[24] J.C. Patterson, S.W. Armfield, Transient features of natural convection in a cavity, J. Fluid Mech 219 (1990) 469–497.
[25] S.W. Armfield, J.C. Patterson, Direct simulation of wave interactions in unsteady natural convection in a cavity, J. Fluid Mech 239 (1992) 195–211.
[26] S.W. Armfield, W. Debler, Purging of density stabilized basins, Int. J. Heat Mass Transfer 36 (1993) 519–530.
[27] S.W. Armfield, R. Janssen, A direct boundary-layer stability analysis of steady-state cavity convection flow, Int. J. Heat Fluid Flow 17 (1996) 539–546.
[28] W. Lin, S.W. Armfield, Numerical prediction of maximum heights of negatively buoyant vertical jets with a weak source in a quiescent homogeneous ambient, in: 13th Australasian Fluid Mechanics Conference, Melbourne, Australia, 13–18 December, 1998, pp. 575–578.